Comparison of Global H I and Hα Line Profiles in MaNGA Galaxy Pairs with FAST

Gaoxiang Jin[1,2] , Y. Sophia Dai[1,5] , Cheng Cheng[1] , Cong Kevin Xu[1] , Jia-Sheng Huang[1,3] , and Lihwai Lin[4]

[1] Chinese Academy of Sciences South America Center for Astronomy (CASSACA), National Astronomical Observatories (NAOC), 20A Datun Road, Beijing 100012, People's Republic of China; ydai@nao.cas.cn

[2] Max Planck Institute for Astrophysics, Karl-Schwarzschild-Str. 1, D-85741, Garching, Germany

[3] Center for Astrophysics | Harvard-Smithsonian, 60 Garden Street, Cambridge, MA 02138, USA

[4] Institute of Astronomy & Astrophysics, Academia Sinica, Taipei 10617, Taiwan

Received 2024 April 9; revised 2025 January 10; accepted 2025 January 11; published 2025 February 20

Abstract

We present case studies comparing the global H I and Hα emission line profiles of six galaxy pairs. The six pairs are selected to have different nuclear activities, with two hosting an active galactic nucleus, and in different merging stages —two of each from the premerging, merging, and postmerging stages. We observe their global H I spectra with the Five-hundred-meter Aperture Spherical radio Telescope, achieving a noise level of ~0.5 mJy. Five out of the six pair systems have secure detections of H I emissions (signal-to-noise ratio > 10). The H I fraction and star formation efficiency of the six pairs do not deviate from isolated galaxies. For the H I line profiles, common unique asymmetry is observed, indicating disturbances of the atomic gas from the galaxy interaction. The global Hα spectra of the merger systems are constructed from the optical integral field spectroscopic observations by integrating the flux in corresponding line-of-sight velocity bins. The Hα spectra tend to show multiple components in the premerger phase and single-component line profiles in the postmerger systems, while all H I spectra show single-component line profiles regardless of merger stages. The H I and Hα spectra show offsets in the central velocities, which appear to decrease from $>100\,\mathrm{km\,s^{-1}}$ in the premerger pair to $<10\,\mathrm{km\,s^{-1}}$ in the postmergers. This trend is consistent with the scenario that, despite the significantly different distributions and kinematics of the atomic and ionized gases, the merging process may contribute to the mixing and eventually align various gas contents.

Unified Astronomy Thesaurus concepts: Galaxy interactions (600); H I line emission (690); Interstellar line emission (844); AGN host galaxies (2017)

1. Introduction

The interstellar medium and circumgalactic medium (ISM and CGM) play important roles in the "baryon cycle" of the galaxy evolution. Observationally, galaxies consume gas through star formation and the accretion of supermassive black holes (SMBHs). The rapid consumption of gas indicates that galaxies have to obtain gas from the CGM (e.g., J. Tumlinson et al. 2017). Also, the observed quenching of massive galaxies proves that there are mechanisms like ram pressure stripping (e.g., J. E. Gunn & J. R. I. Gott 1972) and active galactic nucleus (AGN) feedback (e.g., A. C. Fabian 2012), which can bring the gas away from the host galaxies and then stop the star formation. In simulations, galaxy–galaxy interactions and mergers are the common fast ways for gas to flow into galaxies. The gas inflow may enhance or trigger the star formation (e.g., J. E. Barnes & L. Hernquist 1992) and the fast accretion of SMBHs (known as the AGN) in merging systems (e.g., P. F. Hopkins et al. 2008).

The enhancements of star formation are widely found among interacting and merging star-forming galaxies (SFGs), based on their bluer color (e.g., L. Lin et al. 2007), stronger emission lines (e.g., Y. S. Dai et al. 2021), and luminous infrared emission (e.g., H. S. Hwang et al. 2011). The strongest enhancements seem to occur in the central regions of SFGs

[5] Corresponding author.

(e.g., H.-A. Pan et al. 2019). However, the merger impact on the star formation of individual galaxies is quite complex. Previous works revealed that the merger-triggered star formation enhancement is related to several different parameters, such as the merging stages (e.g., H.-A. Pan et al. 2019), nuclear properties (G. Jin et al. 2021), pair distance (e.g., D. R. Patton et al. 2011), mass ratio (e.g., S. L. Ellison et al. 2008), morphology (C. K. Xu et al. 2010), and bulge masses (C. He et al. 2022). G. Jin et al. (2021) recently revealed that the galaxy–galaxy interaction can enhance the star formation in SFG pairs, but this effect is not significant in narrow-line-selected AGN host galaxies or quiescent galaxies. This difference may be directly related to the galaxy types, particularly their gas abundance, since the narrow-line AGNs and quiescent galaxies are known to be more gas-deficient than SFGs (A. Saintonge et al. 2017; S. L. Ellison et al. 2019).

For nearby galaxies, hydrogen gas is a major contributor to the ISM and CGM. The physical condition, spatial distribution, and kinematics of the hydrogen gas offer information and precious probes for studying the physical and chemical processes during galaxies' evolution. Based on the different temperatures and pressures, hydrogen in the ISM and CGM exists mainly in three phases: the atomic, ionized, and molecular gas. The neutral atomic gas (H I) and ionized gas can be directly measured through the fine-structure emission line at 21 cm and the recombination lines at optical wavelengths, respectively.

H I, as the most abundant and extended gas content in galaxies, is the ideal indicator to study the kinematics of galaxy pair systems. Simulations showed that the tidal forces during galaxy interaction can trigger gas flows into the galaxy center

(e.g., J. E. Barnes & L. Hernquist 1996), while the resulting star formation or AGN activity would quickly consume or blow out the gas. Relevant and detailed observational evidence is still limited. Marginal global H I depletion (~15%) is only found in tens of nearby major mergers (Q. Yu et al. 2022b), while S. L. Ellison et al. (2018) found a 0.3–0.6 dex enhancement of the H I fraction. To investigate the behavior of atomic gas during galaxy mergers, more kinematic information is needed from H I observations. Interferometry studies on nearby interacting mergers found discrepancies between the tidal tails of H I gas and stars (e.g., J. E. Hibbard & J. H. van Gorkom 1996; J. E. Hibbard et al. 2000; D. Iono et al. 2005). But mapping the mass and velocity distribution of H I in galaxies is time-consuming and requires radio interferometry arrays, making it expensive to build statistical galaxy merger samples with high-resolution H I maps. An alternative approach is to estimate the asymmetry from the shape of the global H I line profile through unresolved single-dish observations. For instance, J. Bok et al. (2019) found that galaxy pairs tend to have more asymmetric global H I line profiles. A. B. Watts et al. (2021) and P. Zuo et al. (2022) suggested that although pair and merger systems tend to have unique single-peaked line profiles, there is no significant difference in the quantitative asymmetry distributions. A recent case study also shows that the H I content in a galaxy group can extend to hundreds of kiloparsecs from the group center (C. K. Xu et al. 2022). X. Lin et al. (2023) also found H I stripping in interacting galaxy systems. These complex H I structures and kinematics in groups and pairs can be the reason for the observed global line asymmetry.

Compared to H I, ionized gas is a more direct tracer of star formation, since the hydrogen is mostly excited by the high-energy photons from young stars. These star-forming regions, also known as the H II regions, are the main contributors to the recombination lines in normal galaxies (D. E. Osterbrock & G. J. Ferland 2006). The global line profiles of strong recombination lines, such as Hα, represent the global kinematics of the star formation component. Conventionally, the optical Hα spectra of nearby galaxies are typically observed with narrow slit prisms or thin fibers and are thus either along a certain direction or limited to the central regions of a galaxy. To obtain the global line profile of Hα, optical spectral coverage is needed for the whole galaxy. An integral field unit (IFU) offers the opportunity to build up the optical spectra of a galaxy.

D. R. Andersen et al. (2006) presented a pioneer work of comparing the global H I and Hα line profiles of isolated face-on spirals. The global Hα line profiles are built and tested from the narrowband Hα imaging and the IFU. They found that most of the galaxies show agreement between the global H I and Hα line width, but the line shapes are significantly different, indicating possibly different locations or dynamics. D. R. Andersen & M. A. Bershady (2009) and A. B. Watts et al. (2023) confirmed this conclusion in updated samples and further investigated the origin of the asymmetry in both the global H I and Hα lines. They suggested that the Hα flux distribution typically dominates the asymmetry of the global Hα spectra, and most global H I asymmetries trace disturbances in the outer regions of the host galaxies.

However, such studies are so far limited only to isolated, well-defined face-on galaxies. For galaxy mergers, the comparison between the atomic and ionized gas offers unique insight into the global gas kinematics and distributions during the merger event. It is suspected that the discrepancies between the asymmetry of Hα and H I result from strong perturbations in the galaxy scale, such as galaxy mergers (A. B. Watts et al. 2023).

A sample of galaxy pairs and mergers with both IFU and H I observations can be useful to examine whether galaxy interactions would induce different line profiles between Hα and H I emissions. One of the largest IFU surveys, Mapping the Nearby Galaxies at APO (MaNGA; K. Bundy et al. 2015), has observed ~10,000 nearby galaxies. MaNGA observes the target galaxies out to 1.5 r-band effective radii (R_e), meaning that the fiber bundles can cover most of the stellar and ionized gas component of the galaxies, or in pairs. There is also a large sample of ~1000 merging galaxies observed by MaNGA (H.-A. Pan et al. 2019; G. Jin et al. 2021). We take these advantages and select a pair sample to compare the global H I and Hα line profiles.

H I line profile analysis needs a high signal-to-noise ratio (S/N) as well as enough velocity resolution. For MaNGA galaxies at $z < 0.05$, H I-MaNGA (K. L. Masters et al. 2019) is the ongoing H I follow-up survey. Its data include the proposed new observations using the Robert C. Byrd Green Bank Telescope (GBT) and the archive results from the Arecibo Legacy Fast ALFA (ALFALFA) survey (R. Giovanelli et al. 2005), with a spectral rms of ~1.5 mJy and ~3.5 mJy, respectively (velocity resolution ~10 km s^{-1}). The GBT observation can only reach an S/N of 3 on a $z = 0.02$ galaxy with $M_{H I} = 9.4 M_\odot$. In this paper, we use the Five-hundred-meter Aperture Spherical radio Telescope (FAST; R. Nan 2006) to observe our six pair systems and get deeper observations (rms < 0.5 mJy, $\Delta v = 10$ km s^{-1}, ~3–10× deeper than H I-MaNGA), which is powerful and necessary to analyze the line profile shapes of the H I spectra. Additionally, the large beam size (~2$'$.9) of FAST (P. Jiang et al. 2020) can offer us the global H I line profiles tracing the atomic gas environment of the whole merger systems. Along with the global Hα line profiles constructed from MaNGA, here we present case studies to compare the kinematics of the atomic gas and ionized gas in nearby merging systems.

The paper is constructed as follows. In Section 2, we introduce the target selection and the data product. In Section 3 and Appendix A, we present our FAST data reduction procedure in detail. Section 4 is the scientific analysis, in which we compare the FAST H I spectra with the integrated MaNGA Hα spectra for each galaxy pair system. We measure the H I fraction and the atomic gas star formation efficiency (SFE) and compare them with other H I surveys in Section 5.

Throughout this paper, the velocities are calculated by $c \times z$, where c is the speed of light and $1 + z = \nu_0/\nu = \lambda/\lambda_0$, and then converted to the local standard of rest (LSR) frame. We adopt a cosmology with $H_0 = 70$ km s^{-1} Mpc^{-1}, $\Omega_m = 0.3$, and $\Omega_\Lambda = 0.7$. All stellar masses and star formation rates (SFRs) are based on the Kroupa initial mass function (P. Kroupa 2001).

2. Target Selection and Sample Properties

2.1. MaNGA

MaNGA is one of the main surveys of the fourth generation of the Sloan Digital Sky Survey (SDSS-IV; K. Bundy et al. 2015), which has obtained the IFU spectra for over 10,000 nearby galaxies. The fields of view (FOVs) of the MaNGA science IFUs vary in diameter from 12$''$ to 32$''$, which covers

Table 1
Global Properties of the Six Pair Systems Observed by FAST

Pair ID	Plate IFU	R.A. (deg)	Decl. (deg)	Optical z	BPT Class	M_* log($M_\odot$)	SFR ($M_\odot$ yr^{-1})	Merger Case
(1)	(2)	(3)	(4)	(5)	(6)	(7)	(8)	(9)
A	9194–12701	46.5605	−0.3444	0.0287	SFG	10.01	0.94	Premerging
a	9194–12701	46.5574	−0.3416	0.0294	SFG	9.85	0.87	
B	8254–12701	161.1697	44.0661	0.0258	SFG	10.28	0.36	Premerging
b	N/A	161.1447	44.0413	0.0251	Quiescent	9.71	0.05	
C	8978–12705	249.5586	41.9388	0.0286	AGN	10.74	2.15	Merging
c	8601–1902	249.5576	41.9311	0.0280	Quiescent	10.37	0.02	
D	8241–12705	127.6320	18.2061	0.0269	SFG	10.37	0.88	Merging
E	9507–12704	129.6001	25.7545	0.0182	AGN	10.49	0.92	Postmerging
F	8725–9101	126.8250	46.0326	0.0073	SFG	8.77	0.15	Postmerging

Note. Column (1): galaxies in the same pair are represented by the same letter but in different cases, with the capital letter denoting the more massive member galaxy. Column (2): the MaNGA plate IFU number of the galaxies. Columns (3) and (4): the sky coordinates of the galaxies. Column (5): redshifts derived from SDSS optical spectra. Column (6): BPT classification for the galaxy centers using MaNGA spectra. Columns (7) and (8): global stellar masses and SFRs of the galaxies (or the whole pair systems if the members are not separable). Column (9): the merger stages.

most of the stellar component of our targets. The 2″ fibers have a spatial resolution of ~1 kpc at $z = 0.03$. The spectral resolution ($\lambda/\Delta\lambda$) is about ~2000 at the Hα wavelength (S. A. Smee et al. 2013). Our analysis in this paper is based on the latest public data release, MaNGA Product Launch 11 (the same as SDSS DR17; Abdurro'uf et al. 2022).

Our parent sample is the MaNGA galaxy pair sample used in G. Jin et al. (2021). This parent sample includes 994 IFU-covered galaxies in pairs. Morphologically, the pair systems are visually classified into merger cases from premerging (isolated) to the final coalescence (postmerger). The sample is classified into narrow-line AGNs, composite galaxies, SFGs, and quiescent galaxies based on the emission line ratio diagnostics. Here we refer the reader to G. Jin et al. (2021) for more details about the pair selection, merger stage definition, and AGN classification.

We use the redshifts and stellar masses in MaNGA's parent sample catalog, the NASA–Sloan Atlas.[6] These redshifts are derived from the SDSS spectra, which are observed by single fibers targeting the photometric center of the galaxies. The stellar masses are calculated from the multiwavelength spectral energy distribution fitting (M. R. Blanton & S. Roweis 2007). The photometries used for the fitting include UV bands from the Galaxy Evolution Explorer (GALEX; D. C. Martin et al. 2005) and optical bands from SDSS. The results based on elliptical Petrosian aperture photometries are chosen to reduce the uncertainty due to irregular morphologies of galaxy pairs. The global SFRs are calculated by the attenuation-corrected Hα luminosities, following R. C. Kennicutt & N. J. Evans (2012):

$$\log\left(\frac{\mathrm{SFR}}{M_\odot\ \mathrm{yr}^{-1}}\right) = \log\left(\frac{L_{\mathrm{H}\alpha}}{\mathrm{erg}\ \mathrm{s}^{-1}}\right) - 41.27. \quad (1)$$

The $L_{\mathrm{H}\alpha}$ is based on the integrated spectra in MaNGA's FOV and corrected for attenuation by assuming an intrinsic Hα/Hβ = 2.86 (Case B recombination; D. E. Osterbrock & G. J. Ferland 2006) and the reddening curve from J. A. Cardelli et al. (1989): $L_{\mathrm{H}\alpha} = L_{\mathrm{H}\alpha,\mathrm{obs}} \times [(\mathrm{H}\alpha/\mathrm{H}\beta)_{\mathrm{obs}}/2.86]^{2.36}$. We use the results from the MaNGA Data Analysis Pipeline (F. Belfiore et al. 2019; K. B. Westfall et al. 2019) for the Hα flux and velocity measurements.

---

[6] M. Blanton; http://www.nsatlas.org/.

2.2. Target Selection

For the FAST observations, we selected six pair systems to represent different merging stages and pair types. We restrict the pairs to have spectroscopic redshifts of $z < 0.03$ in order to reach a high S/N and avoid radio frequency interference (RFI) at lower frequencies (P. Jiang et al. 2020). Within 3′, there are no galaxies at similar redshift (i.e., $\Delta v < 2000$ km s^{-1}), which ensures that the pairs are physically isolated in the FAST central beam and the H I observations are not contaminated by nearby sources. To cover different galaxy pairs along the merger sequence and compare the differences, we select two pairs in each merger stage: the premerging stage (weak or no distortion), merging stage (strong distortion), and postmerging stage (coalesced mergers). There are two AGN host galaxies in the merging and postmerging stages, respectively. This selection is made to enable the comparison of the H I line profiles for AGN pairs and non-AGN pairs.

The MaNGA plate IFU numbers, sky coordinates, redshifts, AGN classification results, global stellar masses and SFRs, and merger stages of the six pair systems are summarized in Table 1. Figure 1 shows the global stellar masses and SFRs of the member galaxies in our pairs or the pair systems if not separable. The two AGNs, as well as the SFGs in the pairs, all lie along the star formation main sequence (SFMS) from A. Renzini & Y.-J. Peng (2015).

3. FAST Observation and Data Reduction

3.1. Observational Settings

The FAST observations were carried out in the latter half of 2021 during the shared-risk period (proposal ID: PT2020-0160). We used the L band and the central beam (M01) of the FAST 19-beam receiver to observe the H I emission lines. The systematic performance, such as aperture efficiency, pointing accuracy, and system temperature, has been tested and discussed in P. Jiang et al. (2020). The frequency coverage of the FAST L band is from 1.05 GHz to 1.45 GHz, with a channel resolution of 7.63 kHz (velocity resolution ~1.6 km s^{-1} at $z \sim 0.02$). The average half-power beamwidth of the central beam is ~2′.9. Since the beam size is ~80 kpc in physical size at the targeted redshift, much larger than the sizes

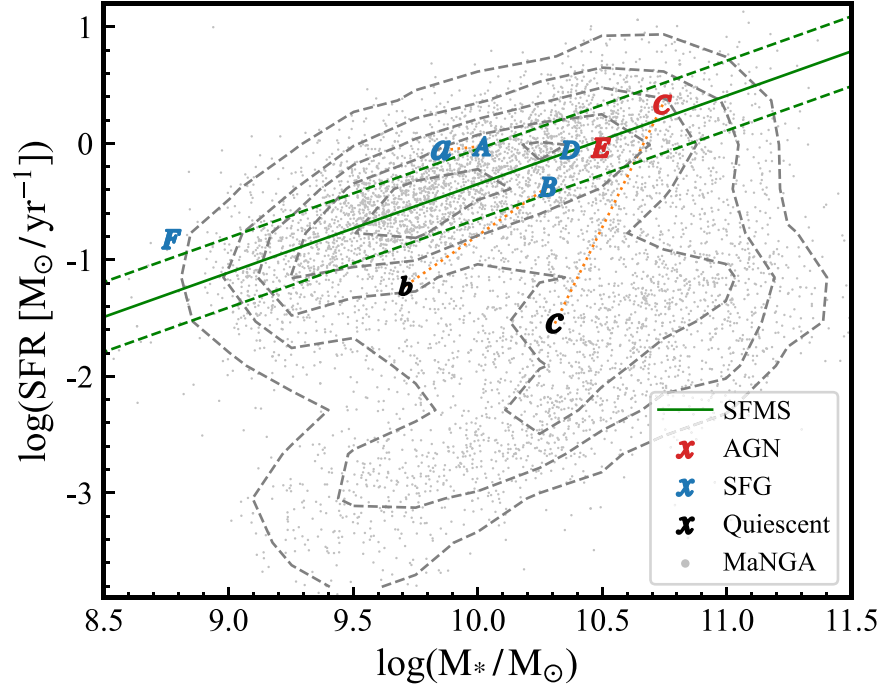**Figure 1.** The stellar masses and SFRs of the galaxies in our six pair systems, overlaid on the overall SFR–M_* distribution (gray dots and contours) of all MaNGA galaxies at $z < 0.05$. The SFMS as well as the typical scatter (± 0.3 dex) are taken from A. Renzini & Y.-J. Peng (2015) and shown in green lines. If separable, the stellar mass and SFR of the two member galaxies in a pair are plotted individually and connected by the orange dotted lines. Galaxies in the same pair share the same symbols and are color-coded by their BPT types.

Table 2
Observational Settings

Pair ID	ON R.A.	ON Decl.	OFF R.A.	OFF Decl.	$t_{\rm Int}$ (s)
(1)	(2)	(3)	(4)	(5)	(6)
Pair A	03:06:14.39	−00:20:37.9	03:04:33.28	−00:31:06.2	1482.9
Pair B	10:44:40.76	+44:03:59.5	10:43:41.05	+44:04:31.0	599.4
Pair C	16:38:14.44	+41:56:33.2	16:41:28.69	+42:00:00.6	2018.2
Pair D	08:30:31.53	+18:12:16.1	08:29:38.14	+18:24:29.9	2377.5
Pair E	08:38:24.12	+25:45:15.0	08:37:36.08	+26:07:56.5	299.0
Pair F	08:27:18.32	+46:02:09.8	08:27:18.04	+46:05:01.1	2400.0

of our pair systems ($<1'$), the H I content outside the central beam is not considered.

We adopt the ON–OFF observation mode, switching every 5 minutes. The ON point of beam M01 is set at the galaxy pair, while the OFF pointings are set at background skies tens of arcminutes away, chosen to have no galaxies at similar redshift. Thus, the OFF pointings can serve as the approximate baselines at the target frequencies. The high-power calibration noise is injected during the first 20 s of each ON–OFF observation.

3.2. Data Reduction

At the time of observation, FAST was still improving its performance, especially the RFI issues, and did not have a finalized data reduction pipeline. We adopted the instrument parameters provided by C. Cheng et al. (2020) and built our own pipeline for our observation settings to reduce the data. Our detailed four-step data reduction procedure can be found in Appendix A and is briefly summarized below. We first manually identify and remove the t-RFI and then perform the temperature calibrations for each exposure; the standing-wave

baseline removal is carried out for the ON-minus-OFF spectra before converting to flux units and smoothing the stacked spectra to measure the H I emissions. The observation settings and spectral properties are listed in Table 2. The integration time ($t_{\rm Intn}$) is the "real" ON duration after removing the time affected by RFI.

The final spectra are shown in Figure 2. After the stacked H I spectra have been obtained, we calculate the H I mass using the relation as first derived by M. S. Roberts (1975). Assuming that the H I emission is optically thin and unresolved by the single-dish telescope beam, the H I mass can be calculated as

$$\frac{M_{\rm H\,I}}{M_\odot} = \frac{2.36 \times 10^5}{(1 + z)^2} \left(\frac{D}{\rm Mpc}\right)^2 \int S(v)\,dv, \qquad (2)$$

where $S(v)$ is the line flux density[7] in janskys and D is the luminosity distance of the galaxy. For nondetections, we

---
[7] Here Jy and Jy beam^{-1} are the same for the flux density since all the sources are unresolved.

Table 3
Observational Results

Pair ID (1)	f_{peak} (mJy) (2)	rms (mJy) (3)	S/N (4)	$\log(M_{H\,I})$ $\log(M_\odot)$ (5)	v_{center} (km s^{-1}) (6)	W_{P50} (km s^{-1}) (7)	$v_{c50,\,H\alpha}$ (km s^{-1}) (8)	$v_{c50,\,H\,I}$ (km s^{-1}) (9)	Δv_{c50} (km s^{-1}) (10)
Pair A	12.26	0.45	24.6	9.96	8816	164	8666	8803	138
Pair B	1.45	0.50	⋯	<8.26	⋯	⋯	⋯	⋯	⋯
Pair C	5.51	0.34	16.2	9.42	8518	142	8465	8503	38
Pair D	4.21	0.29	14.5	9.50	8136	209	8086	8100	14
Pair E	6.83	0.66	10.4	⋯	⋯	⋯	⋯	⋯	⋯
Pair F	17.38	0.46	37.4	8.40	2195	110	2175	2181	6

assume a line width of 300 km s^{-1} and integrate the rms as the upper limit of the H I mass.

The measured and calculated H I properties are listed in Table 3. The S/N is calculated by the ratio of the peak flux (after Hanning smoothing) and the rms. We also compare the sensitivity of FAST with other telescopes in Appendix B. The central H I velocities (v_{center}) are calculated as the mean value of the right and left wing velocities, which are defined as the velocities at 50% of the peak flux for both sides of the emission line. The wing velocity widths (W_{P50}) are defined as the width of the H I line measured at 50% of the peak between both sides, the same as in the H I-MaNGA survey (K. L. Masters et al. 2019). Values of the 50% cumulative flux velocities ($v_{c50,\,H\alpha}$, $v_{c50,\,H\,I}$) are shown in Figures 3, 4, and 5, while Δv_{c50} is the difference between $v_{c50,\,H\,I}$ and $v_{c50,\,H\alpha}$ and will be discussed in Section 4.7.

4. Line Profile Comparison of H I and Hα

In this section, we directly compare the Hα emission line profiles from MaNGA IFU data with the FAST H I line profiles. Below, we perform a case-by-case study of the ionized gas and atomic gas properties in our galaxy mergers.

The H I line profiles of six pair systems are shown in Figure 2, where the velocity resolution is smoothed to ~3.3 km s^{-1}. Compared to the archival H I-MaNGA survey observations (green dashed lines), our results show clear improvements in both S/N and spectral resolution. For the Hα flux density–velocity line profiles, we use all valid spaxels within the whole MaNGA FOV and sum the Hα fluxes in velocity bins of 20 km s^{-1}. The velocity of each spaxel is calculated by $c \times z_{H\alpha}$ and then converted to the LSR frame. We chose the velocity bin of 20 km s^{-1} because D. R. Law et al. (2021) concluded that the MaNGA spectra can provide reliable measurements of astrophysical velocity dispersions $\sigma_{H\alpha}$ ~ 20 km s^{-1}.

The long transition time (~10^7 yr) of the H I line means that the H I line profile represents the Doppler motion of the atomic gas (e.g., J. R. Pritchard & A. Loeb 2012), while the Hα line is more likely to be affected by the other broadening mechanisms; for example, the normal turbulent motions of ionized gas can increase the $\sigma_{H\alpha}$ to ~25 km s^{-1} (e.g., D. R. Andersen et al. 2006), while some violent processes like shock and winds can increase the $\sigma_{H\alpha}$ to $\gtrsim$100 km s^{-1} (e.g., R. L. Davies et al. 2017). So, the Hα fluxes and velocities used for global line profiles are calculated from the Gaussian fit on MaNGA spectra without the velocity dispersion ($\sigma_{H\alpha}$) information. This way, the Hα line profiles can approximately represent the global rotation of the ionized gas and are less affected by broadening

from winds and shocks; thus, they can be compared to the single-dish H I line profiles directly.

For comparison, we then normalize the H I and Hα global line profiles and plot them in the same LSR frame for a direct comparison of the atomic gas and ionized gas flux distribution along the line-of-sight velocities. Here the Hα flux is not corrected for attenuation, since the Hβ line has a low S/N in the galaxy outskirts, making the attenuation correction unreliable. In addition, we check the attenuation (e.g., A_V) calculated from the Balmer decrement and find that the differences between the A_V in the central 2″.5 and the A_V in R_e are around 0.5; thus, the attenuation correction should not affect our global line shape.

Figures 3, 4, and 5 show the comparison of Hα and H I line profiles of the premerging pairs, merging pairs, and post-mergers, respectively. In these figures, the SDSS color images are shown on the right, with the magenta hexagons and white circles representing the MaNGA FOV and FAST beam, respectively. Pair members that are distinguishable are labeled in red text if available. In the main panels, gray lines are H I spectra, and green dashed lines are integrated Hα spectra. The Hα velocity maps are plotted near the spectra, with Hα flux maps shown in black dashed contours. The colors are coded by the velocities, while the color bars are matched to the velocity axis, as an approximate link between the fluxes and the locations in the maps. The upper panels are the cumulative fluxes of Hα and H I. The steeper slope indicates that the fluxes are more concentrative in line-of-sight velocities. The difference of the two 50% flux velocities represents the line-of-sight offset of the ionized and atomic gas.

4.1. Pair A (Figure 3 Upper Panel)

The system includes two SFGs with small projected separation (8.7 kpc) but a larger velocity offset (214.5 km s^{-1}). There is no significant interaction feature, and the two galaxies show regular morphology and velocity maps, indicating that they are likely in the premerger stage.

The MaNGA IFU covered most optical fluxes from both galaxies, and the Hα line profile shows two galaxy components, one rotating disk with the double horn structure and one complex profile with possible differential structures. The rotating disk component is more blueshifted and matched to the brighter galaxy in the lower right. The fainter, bluer galaxy in the upper right shows the complex line profile. These two Hα components are also visually distinct in the velocity map, as well as the optical image, stellar velocity map, and Hα velocity dispersion map (Figure 6), which indicates that these two galaxies are kinematically distinct in the line-of-sight
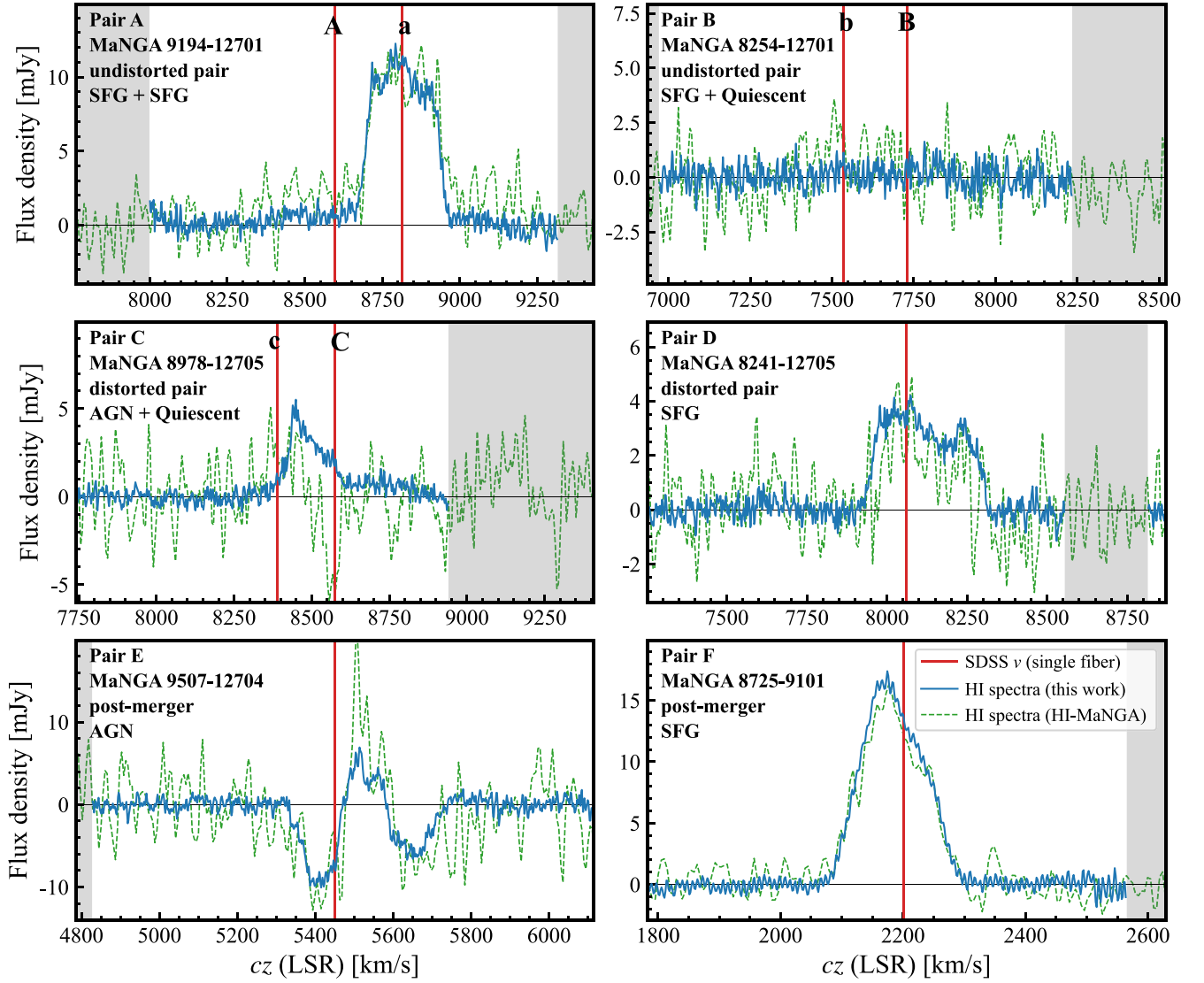
Figure 2. The H I spectra of our six pair systems. In blue are our FAST results with a velocity resolution of about 3.3 km s^{-1}. Red solid lines mark the optical velocities from SDSS single-fiber spectra of the pair member(s), measured at the optical photometric center(s). The redshifts of each member in pairs A, B, and C are also labeled by their pair ID. The frequencies affected by severe f-RFI are masked and shown as gray shaded regions. For comparison, the archival spectra from the H I-MaNGA survey (K. L. Masters et al. 2019) are plotted in green dashed lines. The velocity resolution is ~10 km s^{-1} with a typical on-target integration time of ~1000 s. FAST observations show significant improvement in both the spectral resolution and the S/N.

direction. This also confirms that they are in the premerging phase.

The H I line profile, however, only shows one component, which only matches the velocities of the fainter galaxy. At the velocity of the brighter galaxy, there are marginal signals weaker than 3σ. The difference in the line profiles indicates that the H I content of the pair may be associated with the fainter galaxy. It is not likely that the atomic gas has already mixed together in the premerging stage, because both the H I spectra and the optical morphology do not show any signs of asymmetry or disturbance.

4.2. Pair B (Figure 3 Lower Panel)

This system includes an SFG and a quiescent galaxy with large projected separation (57.2 kpc). This is also a premerging pair system with no significant interaction features. MaNGA covers the SFG and shows global star formation activity.

Although deeper than previous surveys such as H I-MaNGA, we still detect no significant H I signal. The 3σ $N_{\rm H\ I}$ limit is 2.8×10^{18} cm^{-2}. We conclude that this is a relatively H I-poor system including one SFG and one quiescent galaxy. We note that even though the system is not detected for H I, the lower limit of the current atomic SFE is still within the intrinsic scatter of the general SFE distribution (see also Section 5).

4.3. Pair C (Figure 4 Upper Panel)

The system includes a narrow-line AGN with distorted morphology and a quiescent galaxy, covered by two MaNGA IFUs. The clearly distorted morphology indicates that they are in the process of merging.

The Hα flux concentrates near 8350 km s^{-1}, which is associated with a blueshifted star-forming region to the west of the central AGN. The total velocity coverage of Hα, as indicated by the color bar in Figure 4, is about 500 km s^{-1}. The H I line profile is asymmetric, extending over a range of
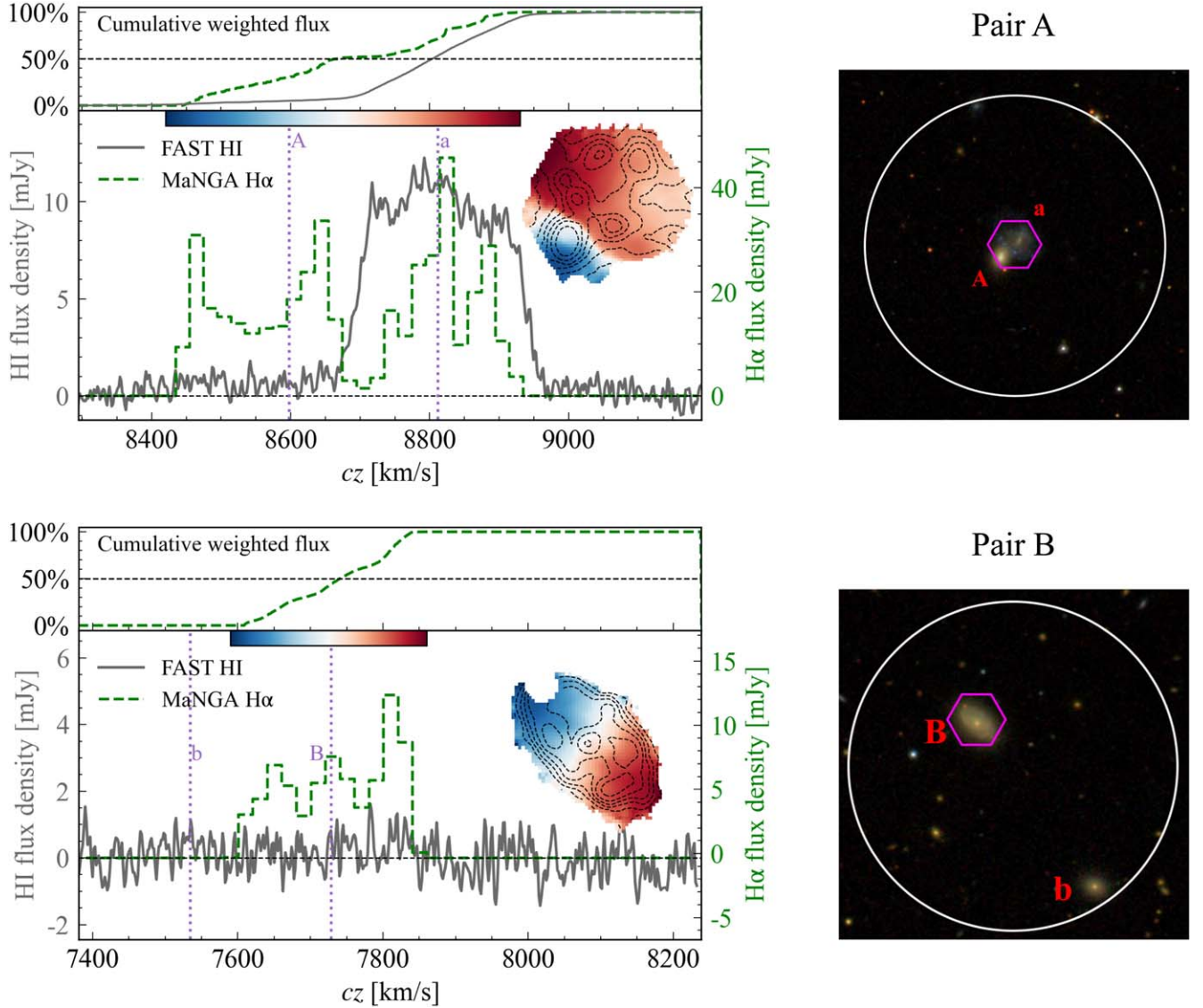
Figure 3. The comparison of global Hα–H I spectra for premerging pairs A and B. Pair B is not detected in H I. The right panels show the SDSS *gri* color image, in which the magenta hexagon represents the MaNGA FOV and the white circle represents the FAST central beam location. The IDs of pair members are labeled near the galaxy positions. In the left panels, the gray lines and the green dashed lines are the cumulative H I and Hα spectra, respectively. The SDSS redshifts are labeled in purple dashed lines, representing the optical velocities at the nuclear positions. The Hα velocity maps from MaNGA are plotted in the panel, color coded by the line-of-sight velocities, with color bars and corresponding velocity ranges shown at the top of each spectrum panel, along the velocity axis. Black dashed contours in the velocity maps are the Hα flux maps. We also plot the cumulative spectra in the upper panels to distinguish the shapes between the two spectra. Their interceptions at the 50% flux can be used to represent the line-of-sight velocity offsets for Hα and H I.

$>400 \, \mathrm{km \, s^{-1}}$, with a long tail toward the red side of higher velocities. The highest peak of H I is $\sim 100 \, \mathrm{km \, s^{-1}}$ offset from the Hα peak, while there is a second peak of H I at $\sim 8550 \, \mathrm{km \, s^{-1}}$, which coincides with the central Hα peak at the same velocity, corresponding to the nuclear region of the AGN. We note that the Hα from the southern galaxy (orange dotted line, amplified by 5 times; Figure 4) is weaker compared to the northern AGN. The extended feature of the H I line profile also matches well with the Hα fluxes at around $8600–8800 \, \mathrm{km \, s^{-1}}$. The seemingly aligned velocity profile longward of $8500 \, \mathrm{km \, s^{-1}}$ may indicate some intrinsic kinematic connection between the Hα and H I components.

The observational star formation law (e.g, R. C. Kennicutt & N. J. Evans 2012) is well known to be a molecular rather than an atomic phenomenon (e.g., F. Bigiel et al. 2008), which disfavors the correlation between Hα and H I on subgalactic scales. But during galaxy mergers, the large-scale disturbance can have a significant impact on the kinematics of all phases of the gas, for instance, redistributing the galaxy in the system toward similar kinematics, which may eventually result in the line-of-sight velocity correlation between Hα and H I. To confirm these implications, higher-resolution radio interferometry observations are needed to confirm this hypothesis.
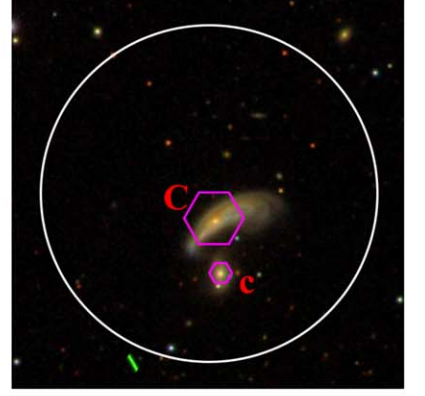
4.4. Pair D (Figure 4 Lower Panel)

The system contains SFGs bridged together with clear tidal features. The morphological connection of the two pair members confirms that they are in the process of merging, probably already after the first encounter.

The wide H I emission, with a width of $\sim 400 \, \mathrm{km \, s^{-1}}$, fully covers and almost doubles the Hα line width ($\sim 200 \, \mathrm{km \, s^{-1}}$). We note that the MaNGA IFU does not fully cover the pair
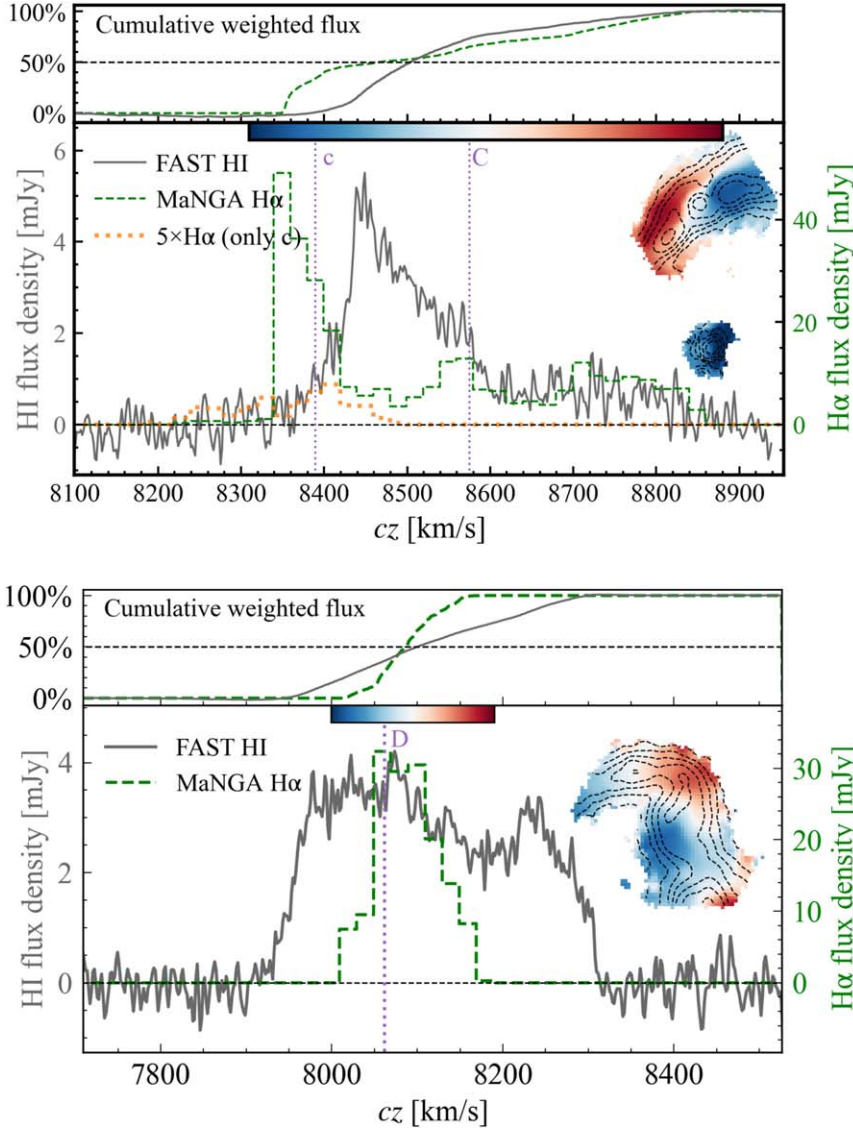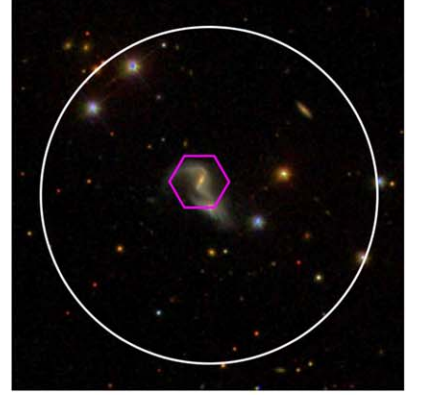
Figure 4. Same as Figure 3. Galaxy c only has a marginal contribution to the overall Hα line profile of the pair system. In the upper panel, the Hα profile from galaxy c is scaled up by a factor of 5 and plotted as the orange dotted line for a better demonstration. The majority of the Hα emission of the system is from the upper right tail of the galaxy (bluer part).

system. The complete Hα line width may be wider than observed if the southern tail extends to high velocity. Based on the Hα velocity profile, the system is encountering volatile kinematics, with the two pair members and the tidal tails showing at several redshift/blueshift components. Similar to pair C, this value is at the high end of the reported H I velocity width distributions in nearby galaxies (e.g., M. A. Zwaan et al. 2010; N. Yu et al. 2022a). Such a high velocity width indicates that either the merging activity strongly disturbed the atomic gas to spread in a wider velocity space, the H I spectra consist of several gas components of overlapping velocities, or a combination of both.

4.5. Pair E (Figure 5 Upper Panel)

This is a clear postmerger system with two long, luminous tidal tails. It is classified as a narrow-line AGN. MaNGA covers the central region, including the merger center and a luminous blue star-forming region.

The Hα components with the highest-velocity component are close to the galaxy nucleus, where $\sigma_{H\alpha}$ also reaches ~300 km s^{-1} (σ_* is only ~180 km s^{-1}), indicating a nucleus-driven line broadening. We also note that the long tails are not covered by MaNGA, and the inclusion of the two tails may further widen the Hα line profile. The H I spectra show two strong, broad absorption features. Given the broad line width of the absorption features in the H I line profile (~400 km s^{-1}), the absorption is possibly associated with the atomic gas related to the AGN and/or merger activities.

Follow-up high-resolution imaging and molecular gas observations are needed to identify the location and origin of the absorption feature. We note that this H I line profile shape, a central emission component with two strong absorption features at both wings, is rare and unique from most well-defined H I absorption galaxies (e.g., K. Geréb et al. 2015). The data reduction procedures are shown in Appendix A, and these features are not from the baseline fitting. The emission and absorption features in the spectrum from FAST observation are consistent with those of the ALFALFA archival observations,
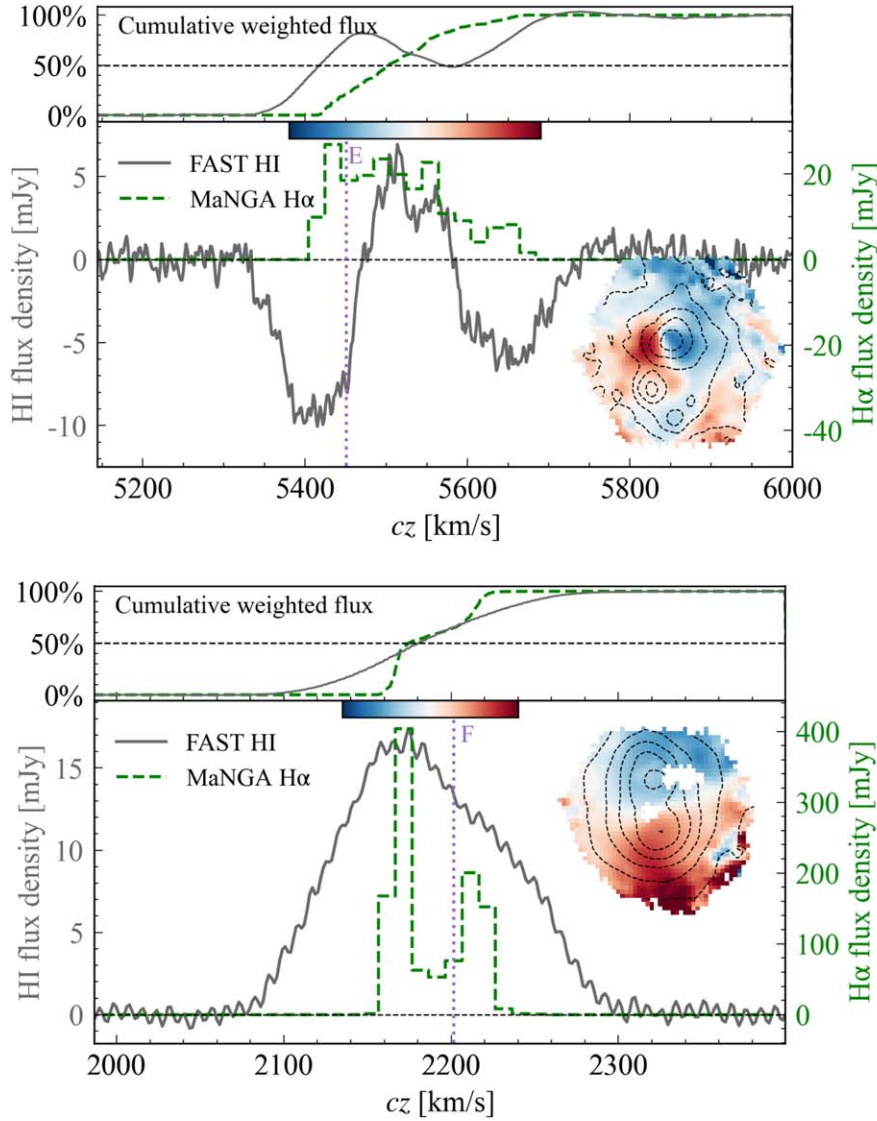
Figure 5. Same as Figure 3 but for postmergers E and F. Pair E shows strong absorption features so that its cumulative H I flux is not monotonically increasing.

and the FAST spectrum shows a higher S/N. We will discuss this object in more detail in an upcoming paper (Y. Dai et al. 2025, in preparation).

4.6. Pair F (Figure 5 Lower Panel)

This is a low-mass postmerger system with two separable nuclei in the optical image, covered in one MaNGA IFU. The two nuclei are both classified as SFGs by the emission line diagnostics.

We can clearly see two Hα components from each galaxy in the flux map (top right corner; contours). The northern nucleus is slightly blueshifted, while the southern nucleus is redshifted from the SDSS reported redshift. The Hα flux map suggests two ionized gas cores around the optical center, and they are not yet fully merged. Thus, although the double-peaked shape of the global Hα spectra could be created by a global rotation, it could also be explained by a mixture of two compact ionized gas cores with different line-of-sight velocities.

Instead of a double-horn shape for typical rotational atomic disks, the H I line profile is centrally peaked. At the velocity of the southern nuclei (~2210 $km\,s^{-1}$), the H I also shows an

excess hump, likely associated with the ionized gas. The line width of the H I (225 $km\,s^{-1}$) is 3 times wider than the Hα (~70 $km\,s^{-1}$, peak-to-peak), confirming the common understanding that the atomic gas is more spread out into the vicinity of the galaxy than the ionized gas that is often bound inside the galaxy (J. F. Navarro et al. 1997). We note that the limited MaNGA IFU size for this system may cause the Hα line width to be underestimated, but the Hα velocity map already shows flattening in the northern and southern regions, indicating that the Hα line is not likely to become as wide as the H I line even with enough IFU coverage.

4.7. Summary of the Comparisons between the Global H I and Hα

In summary, the H I line profiles typically show one continuous component of line width between ~220 and 400 $km\,s^{-1}$ in our sample. A wider H I line profile (~400 $km\,s^{-1}$) is found in pairs undergoing merging or just merged with distorted morphology (C, D, E, F), indicating that the merging process directly affects the atomic gas in their environment. The Hα line profiles, despite the lower velocity resolution, often show velocity components
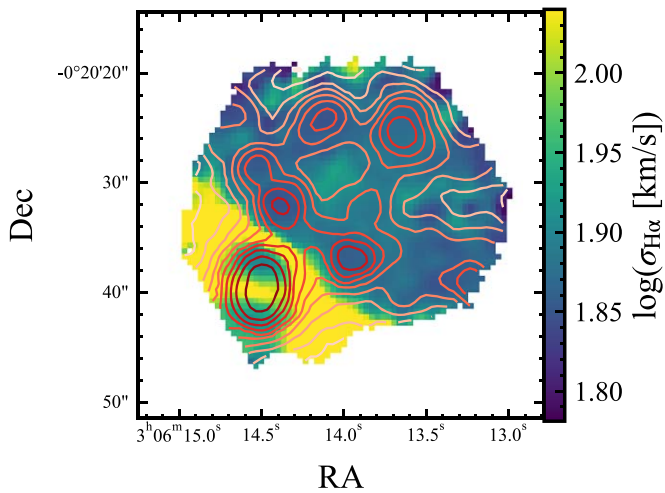
Figure 6. The Hα velocity dispersion map of pair A. The red contours are the Hα flux density map. Despite the velocity differences, the two galaxies show clear different dispersions as well, indicating that the two members in the pair are kinematically distinct.

peaking at one member galaxy or the center of the two member galaxies (A, C, D, F). In most cases, the H I velocity span covers both members, except in pair A, where the H I profile is better aligned with one member galaxy. This SFG–SFG pair seems to be in the premerger case, when the galaxy interaction may not have started yet.

In isolated galaxies, the atomic and ionized gas have been found to share similar kinematics, and the line shape difference could be due to the clumpier Hα distributions, as reported before in D. R. Andersen & M. A. Bershady (2009). Considering that the volatile merging process should affect the gas kinematics in the system, regardless of the gas scale or type (e.g., D. Schiminovich et al. 2013), it is possible that merging would eventually align the atomic and ionized gases.

From a global point of view, we notice that the 50% cumulative flux velocities are generally different between the H I and Hα emissions (Table 3). We note that given the different scales, distributions, and strengths of the ionized and atomic gases, it is normal that the widths, spans, and absolute values of the H I and Hα emission line profiles are different. Therefore, we use Δv_{c50}, the difference between the bulk central velocities of the H I and Hα emissions, as a proxy for the alignment level between the two gas contents. Lower Δv_{c50} values indicate better alignment, and vice versa. We notice that in the premerging case, pair A, Δv_{c50} is ~140 km s^{-1}, though we also note that one ionized gas spectrum does not have H I emission associated with it. As we move toward later merging cases, this value decreases from a few tens of km s^{-1} in merging cases (pairs C and D) to <10 km s^{-1} in the postmerger case (pair F).

Despite our small sample size, this trend suggests that the atomic and ionized gas tend to share similar kinematic centers toward later merging stages. This is consistent with the scenario that the merging process would eventually align and settle the different gas contents down to a common central velocity, possibly as a manifestation of gas concentration.

The overall line profiles of H I and Hα are generally different in all pairs in our sample, except for pair C, in which part of the spectra show some level of overlap. Our results are in general agreement with previous studies that illustrated the environment impact on gases of different phases. For the atomic gas, a galaxy merger or a dense environment can increase the

asymmetry of the spatial distributions (R. A. Angiras et al. 2006, 2007), which has also been confirmed in ionized gases by several spatially resolved studies (e.g., S. Feng et al. 2020; R. S. Bagge et al. 2023).

5. H I Scaling Relations

In this section, we investigate the H I mass properties of the six pairs and compare them to the scaling relations derived from large samples of field galaxies. We note that because the H I observations do not resolve the pair members, the H I mass, stellar mass, and SFR used in this section are the integrated values for the pair system as a whole.

The H I fraction, defined as $\log(M_{H\,I}/M_*)$, is used to estimate the atomic gas abundance of a galaxy. The H I fraction has been widely reported to have a negative correlation with the stellar mass (see A. Saintonge & B. Catinella 2022 for a review), also known as the H I scaling relation. However, the H I scaling relation is found to depend on the survey depth of the derived sample, therefore with different values in the literature. In Figure 7, we compare our mergers with the extended GALEX Arecibo SDSS Survey (xGASS; B. Catinella et al. 2018) representative sample (gray dots and green upper limits), as well as the scaling relation derived from several other surveys. The dashed line is the scaling relation from the 40% ALFALFA survey (S. Huang et al. 2012), which is mostly a local H I-rich sample. The dashed line with filled circles and errors is from a deeper H I survey, xGASS. This scaling relation includes H I nondetections and so can serve as a prediction of H I-normal galaxies. The dashed line with stars is the relation from the galaxies in the Virgo cluster (L. Cortese et al. 2011), representative of the H I-poor galaxies in dense environments.

The pair systems with AGNs are located near the average of xGASS, indicating that they are H I-normal systems, while the SFG mergers show a wide range of H I fractions. The upper-limit SFG pair, pair B, is a H I-poor system. Here we do not include the analysis for pair E, since its H I mass is not constrained due to strong absorption.

The atomic gas SFE, defined as $SFE = SFR/M_{H\,I}$, is a proxy of how efficiently the galaxy can convert the atomic gas to stars. Previous H I surveys have shown that the atomic gas SFE does not significantly evolve with the stellar mass and has an almost constant average value of ~$10^{-9.5}$ yr^{-1} (D. Schiminovich et al. 2010). Some studies also investigate the impact of mergers on atomic gas SFE. For instance, P. Zuo et al. (2018) showed that spiral–spiral galaxy pairs have higher SFE than spiral–elliptical pairs, and Q. Yu et al. (2022b) found higher SFE during the galaxy–galaxy pericentric passage.

As shown in Figure 8, with and without AGN, the pair systems do not deviate significantly from the xGASS sample. For pair B without H I detection, the lower limit of SFE is already ~1σ (~0.5 dex) higher than the average value of the xGASS-detected sample. Considering that the molecular gas is also associated with ongoing star formation activities (e.g., L. Lin et al. 2019), future CO observations would be useful to confirm the SFE and possibly the location of the star formation activities. On the other hand, the other three SFG pairs (A, D, F) lie about 0.3–0.6 dex below the average. This agrees with a scenario that during the galaxy merger, the atomic gas fraction enhancement is more significant compared to the SFR enhancement. A similar phenomenon is also observed for several postmerger samples (e.g., S. L. Ellison et al. 2018), but we need a larger sample to confirm this.
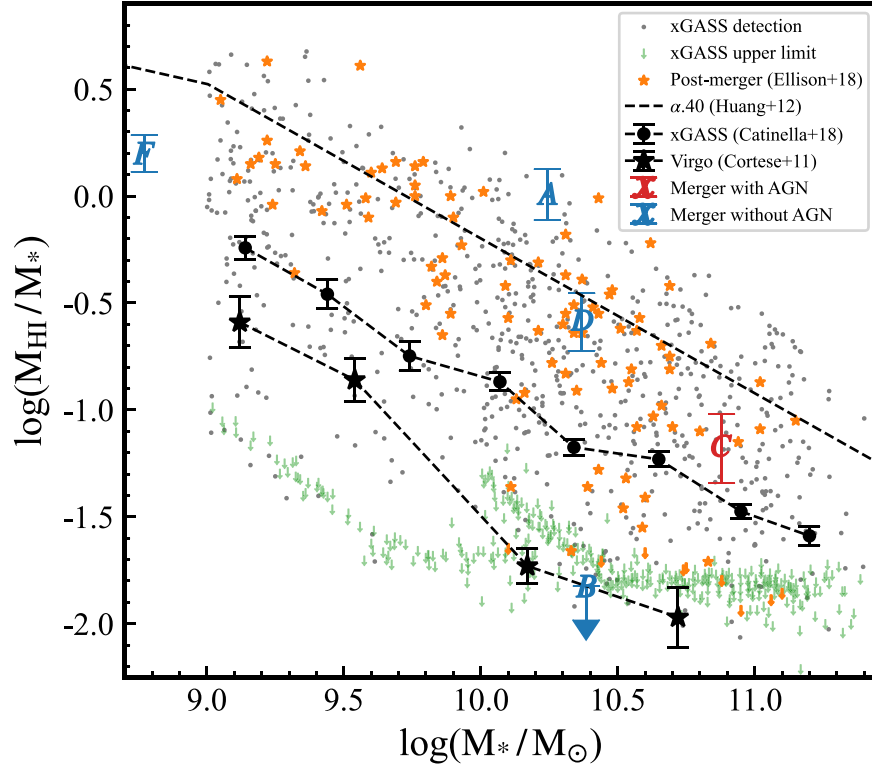
Figure 7. H I fraction vs. stellar mass. We compare the pairs in this paper with statistical samples in different gas environments from large H I surveys, namely, a H I-rich sample from the ALFALFA survey (S. Huang et al. 2012), a H I-normal sample from xGASS (B. Catinella et al. 2018), and a H I-poor sample from the Virgo cluster (L. Cortese et al. 2011). The pair with AGN (C) lies along the H I-rich to H I-normal regions, while the pairs without AGN (A, B, D, F) show a wider range of H I fractions, similar to the postmerger sample (orange stars) in S. L. Ellison et al. (2018).
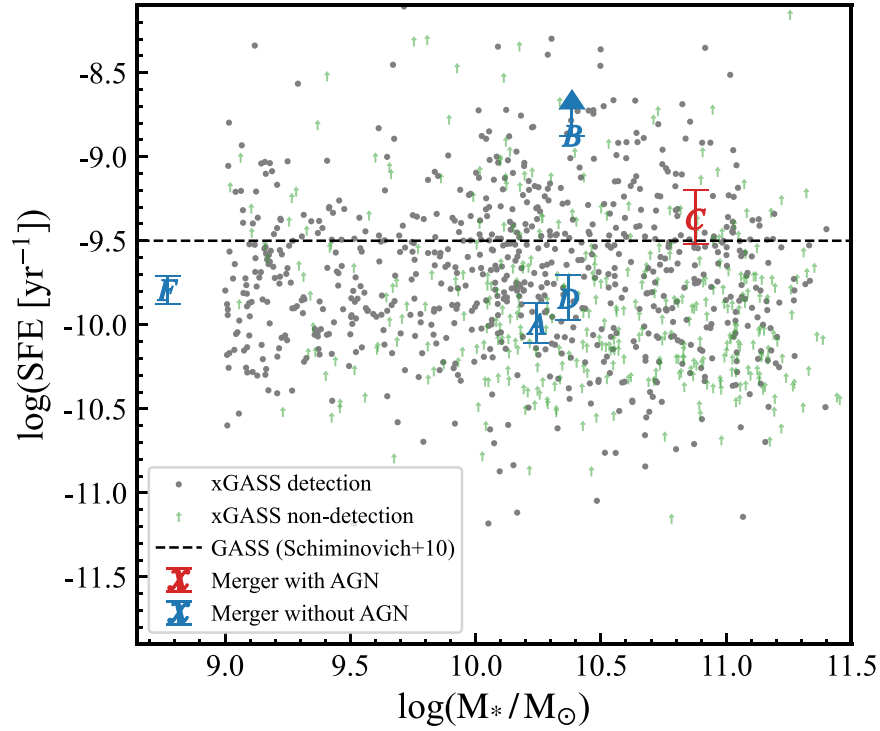
Figure 8. The atomic gas SFE vs. stellar mass. Compared to xGASS (gray dots and green lower limits), the five H I-detected pairs are located in the normal SFE range. The nondetection pair B has a relatively high SFE. The black dashed line shows the average value of the xGASS sample.

6. Summary

This paper presents case studies comparing optical IFU and single-dish radio telescope observations between the Hα and H I emission line profiles in galaxy mergers. We use the FAST telescope to observe the H I for a small sample of six galaxy pairs at different merger stages and different nuclear activities. Five systems are detected with secure H I emissions. Their H I

line profiles all show irregular shapes, such as broadening, asymmetric peaks, and absorption features, which is consistent with archival H I observations of galaxy mergers (e.g., P. Zuo et al. 2022) and addresses the mergers' strong disturbances of the atomic gas. We do not find galaxy pairs at any stage showing two separable H I emission lines in the spectra.

We construct the global Hα line profiles from MaNGA IFU data and compare them with the H I line profiles as a direct approach to compare the ionized gas and the atomic gas. In summary, the line widths and line profile shapes of H I and Hα are different in all five H I-detected galaxy pairs, suggesting that the disturbance of galaxy mergers may have different impacts on the atomic and ionized gases, resulting in unique gas distributions. Along the line-of-sight velocities, however, some peaks or broadening features in the two profiles can match with each other, which is indirect evidence that the ionized and atomic gas have a correlation in at least certain regions. The line-of-sight velocity offset between the H I and Hα emission line centers (Δv_{c50}) shows a decreasing trend toward later merging stages. This tendency indicates that the merging process may contribute to the mixing and eventually align the atomic and ionized gas contents to the same velocity centers. Larger statistical samples are needed to verify this scenario.

The H I fraction and atomic gas SFE of these six pair systems cover wide parameter spaces, and all lie within the 3σ scatter of the large sample results. We do not find evidence that merger or AGN activities have a significant impact on the amount of galaxies' atomic gas.

Compared to the radio interferometry observations, combining optical IFUs and single-dish radio telescopes is an efficient way to study the relative properties of the ionized and atomic gas in galaxies, but this method was only applied in a few works (e.g., D. R. Andersen et al. 2006; D. R. Andersen & M. A. Bershady 2009; A. B. Watts et al. 2023). We expect new, larger statistical samples with both optical IFU and H I observations to study the size, radial distribution, and rotation angle of the atomic gas, and the method presented in this work could serve as an alternative way to analyze the kinematics and distribution of the gas contents of different origins and scales in complex systems like the mergers and pairs.

Appendix A
FAST Data Reduction and Calibration for ON/OFF Mode

We adopt and modify the data reduction and calibration procedure from C. Cheng et al. (2020) and P. Jiang et al. (2020). We summarize and illustrate the procedure in Figure A1, and it is described as follows.

1. *Remove the t-RFI.* We find that the RFI can be divided into two types, the t-RFI and the frequency-domain RFI (hereafter f-RFI). Usually, the t-RFI is strong and will appear or disappear relatively abruptly. The f-RFI usually appears continuously in a narrow frequency range of several MHz and is weaker than the t-RFI; thus, we will remove the f-RFI by masking the relative frequencies later in step 3. In the first step, we manually identify and remove the t-RFI by its strong fluxes, as shown in Figure A1(a). In this way, we get the ON/OFF spectra not affected by t-RFI, as shown in Figure A1(b).

2. *Temperature calibration.* As mentioned in Section 3.1, the calibration noise is injected during the first 20 s of each ON and each OFF exposure. For each 16 MHz frequency bandpass, the antenna temperature profile is calculated as

$$T_{\text{noise,off}}(\nu) = T_{\text{noise,inj}}(\nu) \times \frac{f_{\text{noise,off}}(\nu)}{\bar{f}_{\text{noise,on}}(\nu) - \bar{f}_{\text{noise,off}}(\nu)}, \quad \text{(A1)}$$

where $T_{\text{noise,inj}}(\nu)$ is the injected noise temperature in kelvins; $T_{\text{noise,off}}$ is the temperature with no injected noise, sometimes referred to as the antenna temperature; $f_{\text{noise,off}}(\nu)$ is the mean digital count strength as a function of frequency in the noise-off mode; and $\bar{f}_*$ is the mean digital count strength in the selected frequency ranges for noise-on and noise-off, respectively. In our observations, we use the noise diode noise temperature profile, which was reported to have a temperature varying around 5.4 K for the adopted "high-power" injected calibration

noise at the time of observation (see Section 3.1 of P. Jiang et al. 2020). The choice of averaging the $\bar{f}_*$ is to reduce the influences of f-RFI and signals on the temperature calibration. In this step, we carefully avoid the regions with possible f-RFI signals (as marked in green in Figure A1(c); see below).

In our calibration frequency range of ~16 MHz, the baseline is dominated by the stable standing wave with a ~1 MHz period and thus can be fitted by a polynomial plus a sinusoidal function. As shown in Figure A1(c), we calculate the $\bar{f}(\nu)$ by fitting a (polynomial+sinusoidal) baseline profile to the spectra in the frequency ranges (gray stripes) that are least affected by signals or f-RFI. The top two panels show the spectra for noise-on (blue) and noise-off (red) modes before and after removing the fitted baseline, while the bottom two panels show the resulting $T_{\rm noise,off}(\nu)$ after and before removing the fitted baseline profile. In addition, if the OFF spectra in noise-off mode at the expected H I frequency still show residual values after the baseline removal, we mask the exposure as "failed calibration" and exclude it from the stacking in the next step to make sure that OFF observations can serve as a "no flux" reference. This only applies to a few exposures.

3. *Obtain the spectra from each ON observation.* As shown in Figure A1(d), we select the contiguous OFF spectrum (blue; $T_{\rm OFF}$) as the baseline for each ON observation (red; $T_{\rm ON}$). Then we follow Equation (A2) to obtain the spectra (green spectrum in middle panel) for baseline fitting and f-RFI removal:

$$T_{\rm HI}(\nu) = T_{\rm OFF}(\nu) \times \frac{T_{\rm ON}(\nu) - T_{\rm OFF}(\nu)}{T_{\rm OFF}^-}. \qquad (A2)$$

The middle panel of Figure A1(d) shows the ON–OFF spectra, where the yellow strips are the masked-out f-RFI regions and the light gray strips are the featureless regions used for baseline

fitting. The standing-wave baseline is then fitted in these featureless regions using a polynomial+sinusoidal profile, as plotted in black lines in the middle panel. The standing wave is caused by the reflection between the receiver and the mirror panels and thus has a period of ~1 MHz (~300 m/c). For reliability, we make sure that the baseline fitting frequency regions span at least ~4 MHz (>four sinusoidal periods). The green spectrum in the lower panel is the residual spectrum after removing the fitted baseline and masking out f-RFI regions, i.e., the H I spectrum for one set of ON observations. The temperature is then converted to flux density using the gain profile at the targeted frequencies (P. Jiang et al. 2020), which varies around $16.0\,{\rm K\,Jy}^{-1}$ for all of our targets. When the zenith angle of the source is higher than $26\overset{\circ}{.}4$, the effective aperture of FAST become smaller, resulting in a lower gain. We correct the gain based on the test in P. Jiang et al. (2020) in this step. We derive the spectrum for each ON exposure first, because during each 40 minute observation, the system temperature and the gain of the FAST receiver vary. The rms are calculated from the residual in the featureless gray zones.

4. *Spectral stacking and H I mass.* After we obtain the ON–OFF spectra of all the ON exposures for the same target, we stack the baseline-removed spectra, weighted by their rms. Then the spectra are Hanning smoothed to a velocity resolution of ~3.3 km s^{-1} as our final results. The H I spectra of the six pairs are shown in Figure 2. We find five H I detections with high S/N and one nondetection with low rms to restrict the upper limit of the H I mass (pair B). Green dashed line(s) show the optical redshift(s) of the member galaxies, and the red dashed line corresponds to the center of the detected H I emission line.
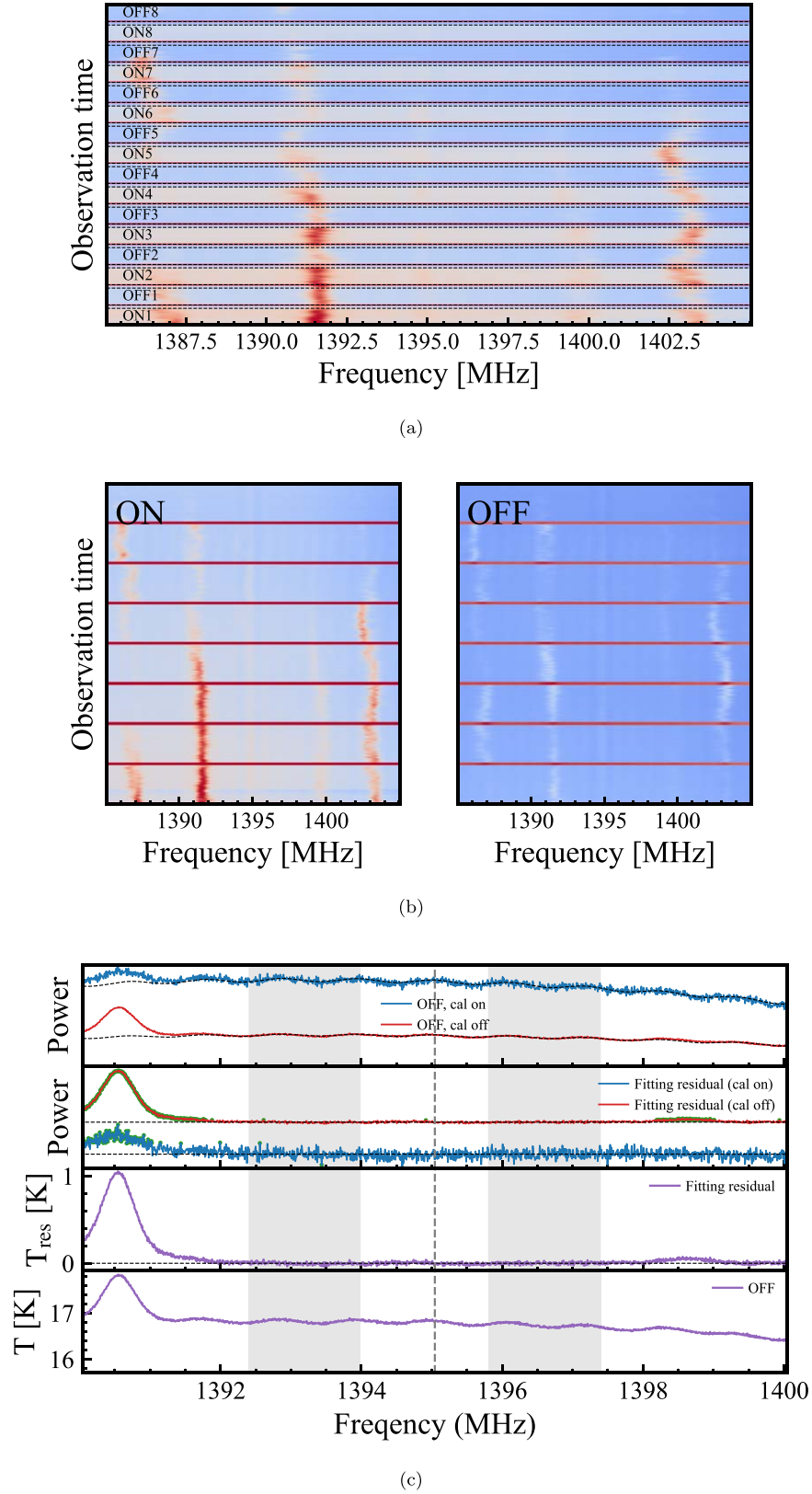
(a)

(b)

(c)

Figure A1. The data reduction procedure adopted in this work, using the data from pair E as an illustration. Step 1 (a): the "waterfall" map of the raw data in a 16 MHz frequency range. The crimson signals are the RFI and calibration noises. Step 2 (b): the "waterfall" maps of combined ON or OFF observations after removing the t-RFI (if it exists). Step 3 (c): example temperature calibration of a 5 minute off-target observation. The gray backgrounds are the selected frequency range with no spectral features used for baseline fitting, and the gray dashed line in the center marks the expected H I frequency from the optical redshift. The first two panels are the noise-on (red) and noise-off (blue) spectra before and after baseline (black curves in the top panel) removal. Green dots in the second panel mark the possible RFI frequencies. Black lines in the second and third panels mark the zero-point baseline. As a check, the third panel shows the resulting temperature profile (purple) combining the noise-on and noise-off observations. The bottom panel is the combined noise-off and noise-on spectra to be used in the next step, after converting the counts into temperatures. Step 4 (d): get the H I spectra (lower panel) from each set of neighboring ON and OFF observations derived in (c). The baseline is fitted (black dashed lines) and removed. Yellow strips mask the frequency range heavily affected by the RFI, and these frequency regions are not used for baseline fitting. Step 5 (e): stacking all H I spectra derived in (d) as the final result. The weight of each exposure is calculated by the rms in the featureless gray zones.
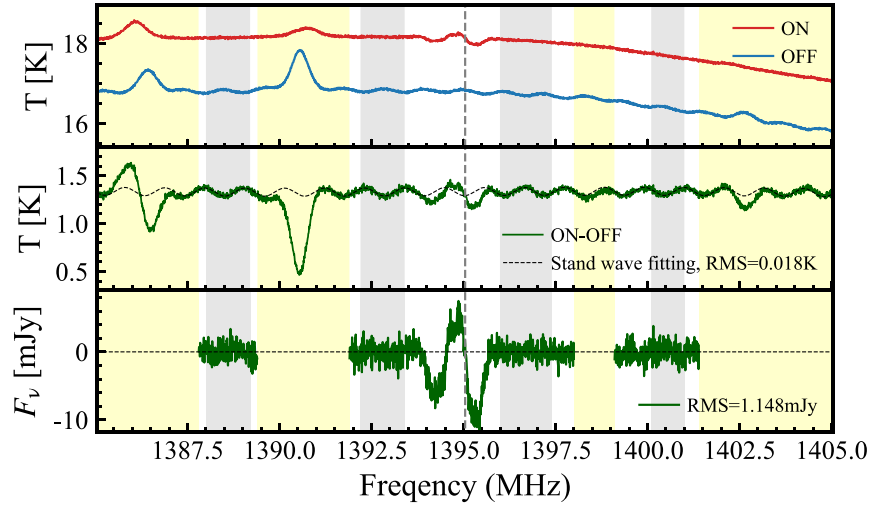
(d)
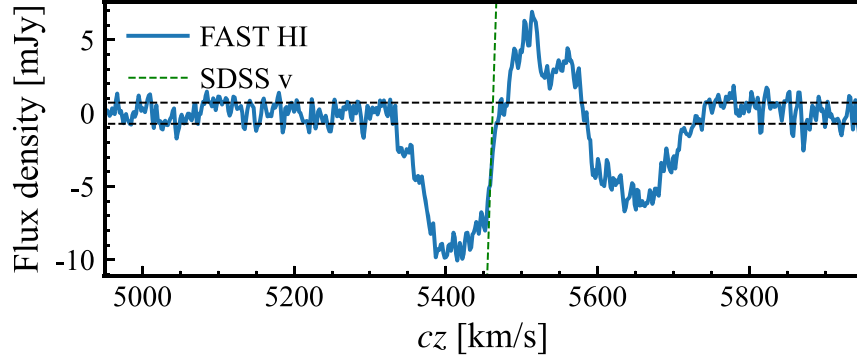
(e)

Figure A1. (Continued.)

Appendix B
The Sensitivity of FAST Compared to GBT and Arecibo

The sensitivity of a single-dish telescope is proportionate to the square of the aperture diameter and also depends on the system temperature. Here we compare the sensitivity of our FAST observation with the GBT and Arecibo observations when using the ON–OFF mode to observe emission lines. For GBT observations, we use the result of the H I-MaNGA survey. For Arecibo observations, we use the results from the GASS survey. They both used the ON–OFF observation mode and share similar data reduction methods with this paper and thus are suitable for comparing the sensitivity. For their observation setups and data reduction, we refer the reader to K. L. Masters et al. (2019) and B. Catinella et al. (2010), respectively.

Here we use the rms when the velocity resolution is converted to $10\,\mathrm{km\,s^{-1}}$ to compare the sensitivity of different telescopes. Ideally, the rms of an observation can be expressed as rms $\propto t^{-0.5} \times dv^{0.5}$. At a given integration time and velocity

resolution, lower rms means higher sensitivity. In Figure B1, we plot the rms versus integration time of the observations from different telescopes. The blue dots, green dots, and red stars are the GBT, Arecibo, and FAST observations, respectively. The black line is the relation used for estimating the rms of a GBT observation. We also plot the $0.3\times$ of the relation as the black dashed line to guide the eyes for comparison. For shorter time observations, the sensitivity of FAST is ~5× better than that of GBT and ~2× better than that of Arecibo. For long-time exposure, however, the rms of FAST observations does not significantly decrease following the theoretical predication. This phenomenon was also found in C. Cheng et al. (2020). One possible reason is found during our data reduction: that the RFI can increase the system temperature, resulting in higher rms. This is the performance of FAST in early 2021. Future improvements are needed for FAST to suppress the rms for the long-time spectral line observation mode.
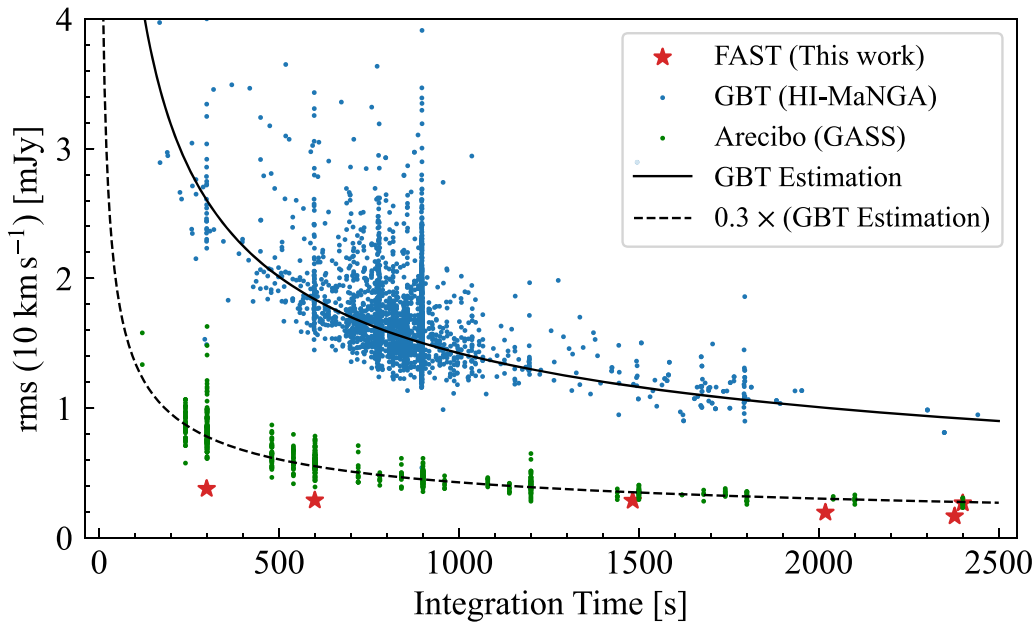
Figure B1. The rms vs. integration times from the H I-MaNGA survey (blue dots), GASS (green dots), and our FAST observations (red stars). All the rms values are corrected to the velocity resolution of 10 km s^{-1}.

ORCID iDs

Gaoxiang Jin https://orcid.org/0000-0003-3087-318X
Y. Sophia Dai https://orcid.org/0000-0002-7928-416X
Cheng Cheng https://orcid.org/0000-0003-0202-0534
Cong Kevin Xu https://orcid.org/0000-0002-1588-6700
Jia-Sheng Huang https://orcid.org/0000-0001-6511-8745
Lihwai Lin https://orcid.org/0000-0001-7218-7407

References

Abdurro'uf, Accetta, K., Aerts, C., et al. 2022, ApJS, 259, 35
Andersen, D. R., & Bershady, M. A. 2009, ApJ, 700, 1626
Andersen, D. R., Bershady, M. A., Sparke, L. S., et al. 2006, ApJS, 166, 505
Angiras, R. A., Jog, C. J., Dwarakanath, K. S., & Verheijen, M. A. W. 2007, MNRAS, 378, 276
Angiras, R. A., Jog, C. J., Omar, A., & Dwarakanath, K. S. 2006, MNRAS, 369, 1849
Astropy Collaboration, Price-Whelan, A. M., & Sipőcz, B. M. 2018, AJ, 156, 123
Astropy Collaboration, Robitaille, T. P., Tollerud, E. J., et al. 2013, A&A, 558, A33
Bagge, R. S., Foster, C., Battisti, A., et al. 2023, PASA, 40, e060
Barnes, J. E., & Hernquist, L. 1992, ARA&A, 30, 705
Barnes, J. E., & Hernquist, L. 1996, ApJ, 471, 115
Belfiore, F., Westfall, K. B., Schaefer, A., et al. 2019, AJ, 158, 160
Bigiel, F., Leroy, A., Walter, F., et al. 2008, AJ, 136, 2846
Blanton, M. R., & Roweis, S. 2007, AJ, 133, 734
Bok, J., Blyth, S. L., Gilbank, D. G., & Elson, E. C. 2019, MNRAS, 484, 582
Bundy, K., Bershady, M. A., Law, D. R., et al. 2015, ApJ, 798, 7
Cardelli, J. A., Clayton, G. C., & Mathis, J. S. 1989, ApJ, 345, 245
Catinella, B., Saintonge, A., Janowiecki, S., et al. 2018, MNRAS, 476, 875
Catinella, B., Schiminovich, D., Kauffmann, G., et al. 2010, MNRAS, 403, 683
Cheng, C., Ibar, E., Du, W., et al. 2020, A&A, 638, L14
Cortese, L., Catinella, B., Boissier, S., Boselli, A., & Heinis, S. 2011, MNRAS, 415, 1797
Dai, Y. S., Malkan, M. M., Teplitz, H. I., et al. 2021, ApJ, 923, 156
Davies, R. L., Groves, B., Kewley, L. J., et al. 2017, MNRAS, 470, 4974
Ellison, S. L., Brown, T., Catinella, B., & Cortese, L. 2019, MNRAS, 482, 5694
Ellison, S. L., Catinella, B., & Cortese, L. 2018, MNRAS, 478, 3447
Ellison, S. L., Patton, D. R., Simard, L., & McConnachie, A. W. 2008, AJ, 135, 1877
Fabian, A. C. 2012, ARA&A, 50, 455

Feng, S., Shen, S.-Y., Yuan, F.-T., Riffel, R. A., & Pan, K. 2020, ApJL, 892, L20
Geréb, K., Maccagni, F. M., Morganti, R., & Oosterloo, T. A. 2015, A&A, 575, A44
Giovanelli, R., Haynes, M. P., Kent, B. R., et al. 2005, AJ, 130, 2598
Gunn, J. E., & Gott, J. R., I. 1972, ApJ, 176, 1
Gunn, J. E., Siegmund, W. A., Mannery, E. J., et al. 2006, AJ, 131, 2332
He, C., Xu, C. K., Domingue, D., Cao, C., & Huang, J.-s. 2022, ApJS, 261, 34
Hibbard, J. E., Vacca, W. D., & Yun, M. S. 2000, AJ, 119, 1130
Hibbard, J. E., & van Gorkom, J. H. 1996, AJ, 111, 655
Hopkins, P. F., Hernquist, L., Cox, T. J., & Kereš, D. 2008, ApJS, 175, 356
Huang, S., Haynes, M. P., Giovanelli, R., & Brinchmann, J. 2012, ApJ, 756, 113
Hwang, H. S., Elbaz, D., Dickinson, M., et al. 2011, A&A, 535, A60
Iono, D., Yun, M. S., & Ho, P. T. P. 2005, ApJS, 158, 1
Jiang, P., Tang, N.-Y., Hou, L.-G., et al. 2020, RAA, 20, 064
Jiang, P., Yue, Y., Gan, H., et al. 2019, SCPMA, 62, 959502
Jin, G., Dai, Y. S., Pan, H.-A., et al. 2021, ApJ, 923, 6
Kennicutt, R. C., & Evans, N. J. 2012, ARA&A, 50, 531
Kroupa, P. 2001, MNRAS, 322, 231
Law, D. R., Westfall, K. B., Bershady, M. A., et al. 2021, AJ, 161, 52
Lin, L., Koo, D. C., Weiner, B. J., et al. 2007, ApJL, 660, L51
Lin, L., Pan, H.-A., Ellison, S. L., et al. 2019, ApJL, 884, L33
Lin, X., Wang, J., Kilborn, V., et al. 2023, ApJ, 956, 148
Martin, D. C., Fanson, J., Schiminovich, D., et al. 2005, ApJL, 619, L1
Masters, K. L., Stark, D. V., Pace, Z. J., et al. 2019, MNRAS, 488, 3396
Nan, R. 2006, ScChG, 49, 129
Navarro, J. F., Frenk, C. S., & White, S. D. M. 1997, ApJ, 490, 493
Osterbrock, D. E., & Ferland, G. J. 2006, Astrophysics of Gaseous Nebulae and Active Galactic Nuclei (Mill Valley, CA: Univ. Science Books)
Pan, H.-A., Lin, L., Hsieh, B.-C., et al. 2019, ApJ, 881, 119
Patton, D. R., Ellison, S. L., Simard, L., McConnachie, A. W., & Mendel, J. T. 2011, MNRAS, 412, 591
Pritchard, J. R., & Loeb, A. 2012, RPPh, 75, 086901
Renzini, A., & Peng, Y.-J. 2015, ApJL, 801, L29
Roberts, M. S. 1975, Radio Observations of Neutral Hydrogen in Galaxies (Chicago, IL: Univ. Chicago Press), 309
Saintonge, A., & Catinella, B. 2022, ARA&A, 60, 319
Saintonge, A., Catinella, B., Tacconi, L. J., et al. 2017, ApJS, 233, 22
Schiminovich, D., Catinella, B., Kauffmann, G., et al. 2010, MNRAS, 408, 919
Schiminovich, D., van Gorkom, J. H., & van der Hulst, J. M. 2013, AJ, 145, 34
Smee, S. A., Gunn, J. E., Uomoto, A., et al. 2013, AJ, 146, 32
Tumlinson, J., Peeples, M. S., & Werk, J. K. 2017, ARA&A, 55, 389
Watts, A. B., Catinella, B., Cortese, L., Power, C., & Ellison, S. L. 2021, MNRAS, 504, 1989
Watts, A. B., Cortese, L., Catinella, B., et al. MNRAS 2023, 519, 1452

Westfall, K. B., Cappellari, M., Bershady, M. A., et al. 2019, AJ, 158, 231
Xu, C. K., Cheng, C., Appleton, P. N., et al. 2022, Natur, 610, 461
Xu, C. K., Domingue, D., Cheng, Y.-W., et al. 2010, ApJ, 713, 330
Yu, N., Ho, L. C., Wang, J., & Li, H. 2022a, ApJS, 261, 21

Yu, Q., Fang, T., Feng, S., et al. 2022b, ApJ, 934, 114
Zuo, P., Ho, L. C., Wang, J., Yu, N., & Shangguan, J. 2022, ApJ, 929, 15
Zuo, P., Xu, C. K., Yun, M. S., et al. 2018, ApJS, 237, 2
Zwaan, M. A., Meyer, M. J., & Staveley-Smith, L. 2010, MNRAS, 403, 1969